Check for updates

ARTICLE　OPEN

The innate interfacial elastic strain field of a transformable B2 precipitate embedded in an amorphous matrix

Xiaoling Fu [1,10 ✉], Yujun Lin[1,10], Mixun Zhu[1,10], Kai Wang[1], Jiaqing Wu[1], Xing Tong[2], Wenli Song[3,4], Ming Jen Tan [5], Yuanzheng Yang[1], Jun Shen[6], Gang Wang[7], Chan Hung Shek [8] and Robert O. Ritchie [9 ✉]

When a transformable B2 precipitate is embedded in an amorphous matrix, it is often experimentally observed that the crystalline-amorphous interface not only serves as an initiation site for the martensitic transformation due to local stress concentrations, but also as an inhibitor to stabilize the transformation, the latter being attributed to the "confinement effect" exerted by the amorphous matrix, according to the Eshelby solution. These two seemingly incongruous factors are examined in this study using molecular dynamics simulations from an atomic interaction perspective. An innate strain gradient in the vicinity of the crystalline-amorphous interface is identified. The actual interface, the compressive/dilatative transition, and the interfacial maximum strain are investigated to differentiate from the conventional "interface" located within a distance of a few nanometers. Our innate interfacial elastic strain field model is applicable for the design of materials with a higher degree of martensitic transformation and controllable stress concentration, even in cryogenic environments.

INTRODUCTION

To solve the problem of the extreme brittleness of monolithic metallic glasses, one approach has been to add precipitates into the amorphous matrix to impede the propagation of shear bands, thereby delaying the fracture process and achieving better plasticity[1–5]. However, under tension loading, non-transformable precipitates embedded in an amorphous matrix usually lead to strain softening[6–8], although phase transformable (shape-memory) inclusions in bulk metallic-glass composites (BMGCs) do display work hardenability ascribed to "transformation-induced" work hardening and plasticity[9–17]. Indeed, recent experimental studies reveal that shape memory BMGCs can display even higher strength[18–20], ductility[18,19], better work hardenability[18–20] and impact toughness[21] at cryogenic temperatures, which is ascribed to an enhanced transformed fraction of austenite precipitates (Supplementary Note 1). All of the above phenomena have been ascribed to the "confinement effect" or "hydrostatic pressure" exerted on the transformable B2 phase at cryogenic temperatures by the amorphous matrix, according to the classical Eshelby solution[22] (Supplementary Note 2, Supplementary Fig. 1). It has also been widely accepted that the stress/strain concentration at the interface is related to the elastic modulus mismatch[13,23,24] which promotes shear band initiation and stress/strain-induced martensitic transformation[25,26] (based on in situ tension tests within the scanning electron microscope). The manipulation of the transformed fraction of austenite and stress concentration clearly can play a decisive role in affecting work-hardening capability and shear band initiation. However, the puzzling question is how one interface can act in two seemingly contradictory roles to affect both martensitic transformation and shear band nucleation.

The Eshelby solution[22] is valid for isotropic ellipsoidal inclusions in an isotropic infinite body, which assumes a uniform stress and strain inside the whole inclusion and the same elastic moduli for the matrix and inclusion, as described in Supplementary Note 2. Many experimental[27–29] and simulation studies[30,31] for B2-NiTi alloys surrounding Ni_4Ti_3 precipitates suggest that the Eshelby solution may not be sufficient since the two assumptions cannot always meet the actual situation (Supplementary Note 3). To resolve this issue, in this study Molecular Dynamics (MD) simulations based on interatomic potentials were performed as they should accurately reveal the inhomogeneous elastic fields from the spontaneous behavior of the atoms. Further, to understand the strain field adjacent to the crystalline-amorphous interface, a model comprising a transformable spherical B2 nanoparticle of varying sizes in an amorphous matrix was built to quantitatively investigate the intrinsic interfacial elastic stress/strain field distribution responsible for this phenomenon.

RESULTS

Strain fields caused by B2 precipitates of different sizes

The material under investigation was a spherical B2 CuZr precipitate embedded along the crystallographic directions of [100], [010] and [001] in a $Cu_{50}Zr_{50}$ amorphous matrix with side length of 23 nm (Fig. 1). The model construction is detailed in the Methods section. The intent here is to quantitatively examine the innate interfacial strain distribution and its impact on the martensitic transformation in BMGCs using MD. The yellow colored region in Fig. 1a–c is the crystalline B2, while the blue-red colored area represents the amorphous matrix. The configuration of the initial unrelaxed structure and relaxed structure are compared in Fig. 1c. The diameters of the B2 particles after

[1]School of Materials and Energy, Guangdong University of Technology, Guangzhou 510006, China. [2]Songshan Lake Materials Laboratory, Dongguan 523808, China. [3]Institute of High Energy Physics, Chinese Academy of Sciences (CAS), Beijing 100049, China. [4]Spallation Neutron Source Science Center, Dongguan 523803, China. [5]Singapore Centre for 3D Printing, School of Mechanical and Aerospace Engineering, Nanyang Technological University, Singapore 639798, Singapore. [6]School of Materials Science and Engineering, Fujian University of Technology, Fuzhou 350118, China. [7]Institute of Materials, Shanghai University, Shanghai 200444, China. [8]Department of Materials Science and Engineering, City University of Hong Kong, Kowloon Tong, Hong Kong SAR, China. [9]Department of Materials Science & Engineering, University of California, Berkeley, CA 94720, USA. [10]These authors contributed equally: Xiaoling Fu, Yujun Lin, Mixun Zhu. ✉email: fuxiaoling@gdut.edu.cn; roritchie@lbl.gov

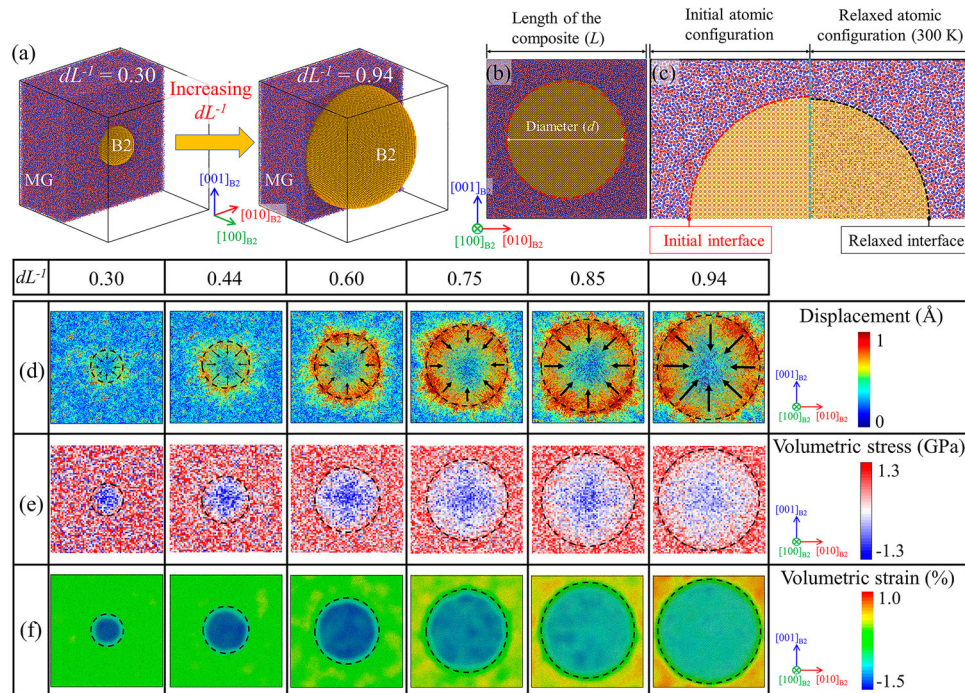**Fig. 1 The distribution of atomic displacements, volumetric stress and volumetric strain within the 3D composite model. a** 3D Configuration of a spherical B2 nanoparticle embedded in an amorphous matrix; (**b**) 2D configuration of the composite; d is the diameter of nanoparticle and L is the total length of the composite; (**c**) Cross-section of a quadrant of the composite (the left part is the initial unrelaxed structure, the right part is relaxed structure at 300 K). The red dashed line indicates the initial crystalline-amorphous interface, while the black dashed line represents the crystalline-amorphous interface after relaxation. **d** Non-affine atomic displacements (Black arrows indicate the displacement direction of atoms), (**e**) heatmaps of the volumetric stress averaged in 70×70 grid; and (**f**) Volumetric strain fields of the composites with different dL^{-1} values after relaxation at 300 K.

relaxation of the BMGCs were designed to vary from 6.9 nm, 10.0 nm, 13.8 nm, 17.2 nm, 19.6 nm to 21.5 nm. The relative length of the particle size d to the length L of composite is defined as the normalized particle diameters dL^{-1}, which were correspondingly 0.30, 0.44, 0.60, 0.75, 0.85, 0.94, respectively.

After relaxation, the crystalline-amorphous interface (red dashed line in Fig. 1c) shifts towards inside of the B2 nanoparticle (black dashed line in Fig. 1c). The average atomic volume changes of the B2 precipitate, amorphous matrix and BMGCs with various precipitate sizes are described in Supplementary Note 4, Supplementary Table 1 and Supplementary Fig. 2. For all BMGCs, the amorphous matrix expands and the B2 precipitate contracts. The smallest precipitate will contract the most, while the amorphous matrix embedded with the largest precipitate will expand the most. As the dL^{-1} increased gradually from 0.30 to 0.94, the displacement of atoms near the crystalline-amorphous interface increased from roughly 0.5 Å to 1.0 Å (Fig. 1d). This is similar to the results of Lyu et al.[32] that the displacement of interfacial atoms increases as a function of the sphere radius. The black arrows indicate that atoms at the interface move towards the interior of the B2 particles. This observed deviation phenomenon of the interfacial atoms from the standard cubic B2 lattice is consistent with Wu et al.[33]'s in situ neutron diffraction and simulation work.

Figure 1e, f respectively present contour maps of the atomic stress and strain fields inside the composites. The central atoms of the B2 particles experience a compressive stress/strain, whereas the amorphous region is generally under a tensile stress/strain. The specimen with the smallest precipitate size experiences the highest compressive stress and strain inside the B2 particle (the blue color region in Fig. 1f), while BMGCs containing the largest particles experience the highest tensile strain in the amorphous region (the red color region in Fig. 1f). This is consistent with our

average atomic volume estimates. The smallest B2 particle contracts the most and undergoes the highest compressive strain. The amorphous matrix embedded with the largest precipitates expands the most and therefore experiences the highest dilatative strain. In general, the area that lies adjacent to, but not exactly at, the crystalline-amorphous interfaces (black dashed line in Fig. 1f) displays a relatively higher strain, which conforms to the highest interfacial displacement being adjacent to the interface (Fig. 1d).

The characteristic points of the strain distribution in Fig. 1f are illustrated in Fig. 2a. We emphasize that the locations of the points of compressive/dilatative and the interfacial maximum strain ($\varepsilon_{\text{max-interface}}$) are different from the conventional crystalline-amorphous interface. The distance between the compressive/dilatative point and the interface is designated as "b", while the span between the interfacial maximum strain and the interface is termed "a". Figure 2b shows the strain distribution along the central axis in the $[100]_{B2}$ or $[010]_{B2}$ direction. The compressive volumetric strain is the largest at the center of the B2 particles, then gradually increases to zero; at the latter point a transition from compression to dilatation can be seen in all specimens a few Ångstroms from, or even closer to, the crystalline-amorphous interface. The dilatational strain continuously increases to a maximum value (indicated as $\varepsilon_{\text{max-interface}}$ in Fig. 2a), which is also located a few Ångstroms from the crystalline-amorphous interface inside the amorphous matrix for all specimens. After reaching a maximum tensile value, the strain fluctuates and tends to recede to the bulk level, although still in the tensile direction.

The detailed information in Fig. 2b is shown in Supplementary Note 5 and Supplementary Fig. 3a–f, which display the strain distribution for various "dL^{-1}" values one by one. When dL^{-1} increases from 0.30 to 0.94, the "b" value gradually decreases from 1.39 nm to −0.06 nm (Supplementary Table 1, Supplementary Fig.
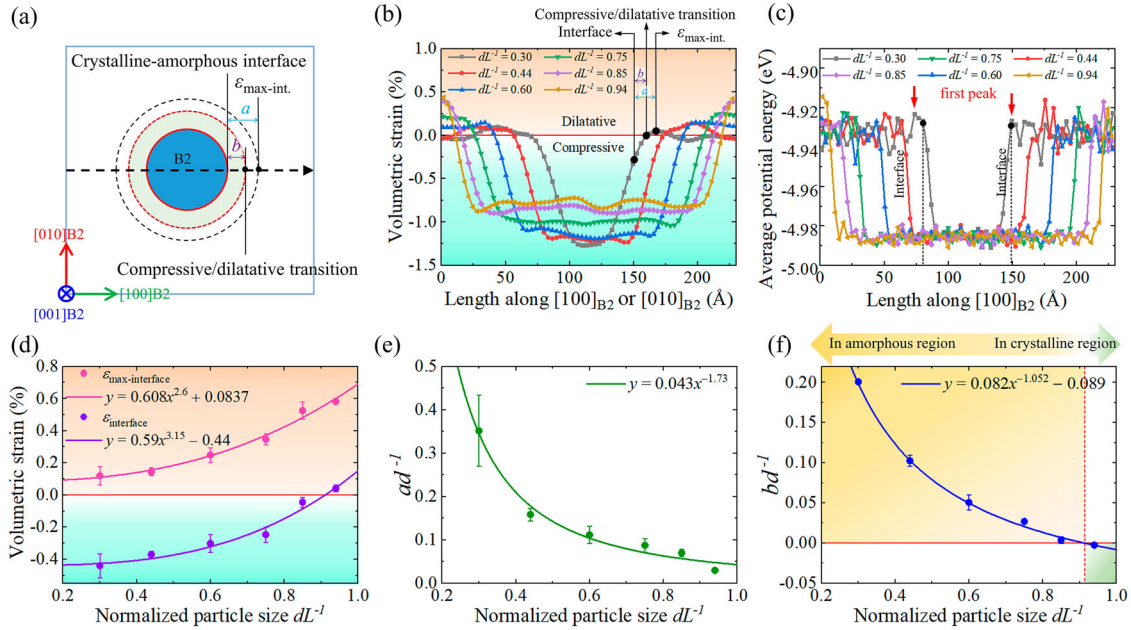
Fig. 2 The relative distances among the compressive/dilatative transition, the exact interface and the interfacial maximum strain. Schematic illustration of the embedded B2 nanoparticle in an amorphous matrix (as sketched at (**a**)) of configurations with various particle diameters: *a* is the distance between the interface and the interfacial maximum strain, *b* is the span between the interface and the position of compressive/dilatative transition; positive (negative) value of "*b*" indicates that the compressive/dilatative transition is inside the amorphous (crystalline) phase; (**b**) volumetric strain distributions along $[100]_{B2}$ or $[010]_{B2}$; as the atomic strain fluctuates, to have the best visualization effect, the volumetric strain distribution were illustrated along the $[010]_{B2}$ direction for $dL^{-1} = 0.30$, while the others were along the $[100]_{B2}$ direction for $dL^{-1} = 0.44$, 0.60, 0.75, 0.85, and 0.94; (**c**) average potential energy distributions along the central axis in $[100]_{B2}$; (**d**) The strain at the interface ($\varepsilon_{interface}$) and the maximum interfacial strain($\varepsilon_{max\text{-}interface}$); (**e**) the ratio of distance "*a*" to the particle diameter *d*, ad^{-1}, as a function of the normalized particle size dL^{-1}; (**f**) the ratio of distance "*b*" to the particle diameter *d*, bd^{-1}, as a function of the normalized particle size dL^{-1}. Note that the values of $\varepsilon_{interface}$, $\varepsilon_{max\text{-}interface}$, *a* and *b* were calculated based on the average value of strain along the [100], [010] and [001] directions of the B2 crystal in Fig. 2d–f. $\varepsilon_{max\text{-}int.}$ is the abbreviated form of $\varepsilon_{max\text{-}interface}$. Bars represent standard deviation of the mean.

3a–f), indicating that the compressive/dilatative transition region moves from outside the B2 precipitate (Supplementary Fig. 3a–e) to merge with the "exact" interface, before staying inside the precipitate (Supplementary Fig. 3f). The "*a*" value decreases from 2.43 nm to 0.64 nm as the "dL^{-1}" increases from 0.30 to 0.94, indicating that the interfacial maximum strain is always a few Ångstroms away from the "exact" interface. The average potential energy for the central axis along the $[010]_{B2}$ or $[100]_{B2}$ direction (Fig. 2c and Supplementary Fig. 4) generally matches with the strain distribution profile displayed in Fig. 2b and Supplementary Fig. 3. This configuration is consistent with the MD results of Shi et al.[34], described in Supplementary Note 6.

The interfacial maximum strain ($\varepsilon_{max\text{-}interface}$), the strain at the exact "interface" ($\varepsilon_{interface}$), the relative width between the interface and the position of the interfacial maximum strain (ad^{-1}), and the relative position of the compressive/dilatative transition (bd^{-1}), all as a function of dL^{-1} (Fig. 2d–f), can be expressed as follows:

$$\varepsilon_{interface}(\%) = 0.59\left(\frac{d}{L}\right)^{3.15} - 0.44, \tag{1}$$

$$\varepsilon_{max\text{-}interface}(\%) = 0.608\left(\frac{d}{L}\right)^{2.6} + 0.0837, \tag{2}$$

$$\frac{b}{d} = 0.082\left(\frac{d}{L}\right)^{-1.052} - 0.089, \tag{3}$$

$$\frac{a}{d} = 0.043\left(\frac{d}{L}\right)^{-1.73}, \tag{4}$$

where *a* is the length between the interface and the position of interfacial maximum strain, and *b* is the span between interface and the position of the compressive/dilatative transition. As particle size increases, both $\varepsilon_{interface}$ and $\varepsilon_{max\text{-}interface}$ increases. The interfacial maximum strain $\varepsilon_{max\text{-}interface}$) is always higher than $\varepsilon_{interface}$ for all BMGCs (Fig. 2d). Both *a* and *b* decrease accordingly as the "dL^{-1}" increases (Fig. 2e, f). When dL^{-1} increases from 0.30 to 0.94, the value of "*b*" is reduced from ~1.39 nm to −0.06 nm, and the value of "*a*" decreases from 2.43 nm to 0.64 nm. At $dL^{-1} = \sim 0.91$, the interfacial strain $\varepsilon_{interface} = 0$ (Fig. 2c, f), the compressive/dilatative transition merges with the "exact" interface. The rationality of "*b*" and "*a*" is presented in Supplementary Note 7.

Temperature-induced martensitic transformation (MT)
The total potential energies on cooling were calculated to obtain M_s (martensite start) temperatures for all specimens (Fig. 3a). In previous investigations for NiTi-based alloys[31,35], the potential energy has been generally considered to be a good indicator of the transformation. While cooling from 500 K to 70 K, the potential energy linearly decreases before a "sudden drop" occurs; this drop, which corresponds to M_s, is presented in Fig. 3b. When the particle size dL^{-1} decreases from 0.94, 0.86, 0.75, 0.60, 0.44 to 0.30, the M_s temperature declines linearly from 190 K, 178.5 K, 176.5 K, 161.4 K, 154.8 K to137.0 K, respectively. The enlarged view of this "sudden drop" for small particles (where dL^{-1} values are 0.30, 0.43 and 0.60) is presented in Supplementary Fig. 5. Our measured M_s temperatures agree reasonably well with the differential scanning calorimetry and in situ high-energy synchrotron X-ray diffraction (HEXRD) results
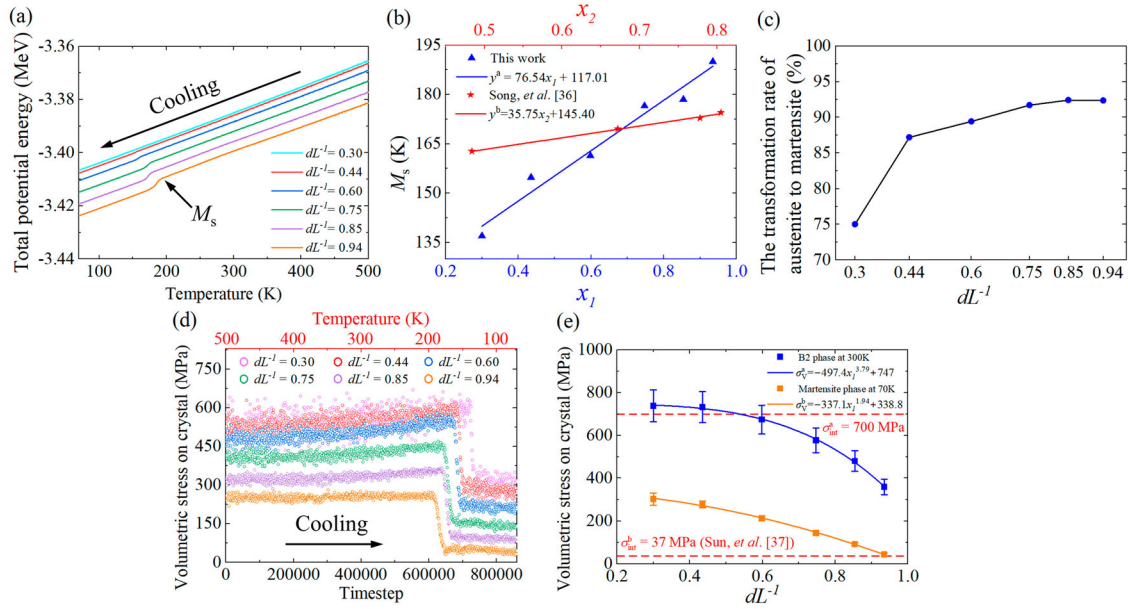
Fig. 3 The variations of total potential energy and volumetric stress associated with martensitic transformation behavior. a Evolution of total potential energies calculated with various dL^{-1} values; (**b**) M_s temperatures obtained from the total potential energy change (blue triangle symbols), which were compared with the experimental data (red star symbols) measured by differential scanning calorimetry and in situ synchrotron X-ray diffraction[36]; $x_1 = dL^{-1}$, x_2 represents volume fraction of nanocrystals. Note that the x_1 does not have a corresponding relationship with x_2. **c** The rate of the initial B2 austenite to martensite transformation as a function of dL^{-1} after cooling. **d** Evolution of the volumetric stress of all B2 crystalline atoms with different dL^{-1} values from 500 K to 70 K as a function of timestep and temperature. A "sudden drop" phenomenon was observed as the temperature decreases for every specimen. Each starting point of the "sudden drop" of the volumetric stress corresponds to the M_s of the specimens. **e** Volumetric stress of all crystal atoms as a function of dL^{-1}. The volumetric stress is the sum of all atoms of inclusions. It includes all atoms of the crystalline phase, which can be under either compressive or dilatative stress. It is an estimated comparison with the "hydrostatic pressure" from the Eshelby solution calculated by Sun et al.[37] (red dash line). σ_{int}^a ($= 700$ MPa) is the "hydrostatic pressure" before the martensitic transformation; σ_{int}^b ($= 37$ MPa) is the "hydrostatic pressure" after the martensitic transformation. Bars represent standard deviation of the mean.

of Song et al.[36]. These authors reported measurements of decreased M_s temperatures from 174.5 K, 172.8 K, 169.5 K to 162.7 K (represented by "red star" symbols in Fig. 3b) for $Cu_{47.5}Zr_{47.5}Al_5$ composites containing B2 with respective volume percentages of 80.5%, 77.8%, 67.2% and 48.4%. The volumetric stresses of all crystalline atoms were computed as a function of timestep (Fig. 3d), temperature (Fig. 3d) and dL^{-1} (Fig. 3e), with the detailed methods of calculating volumetric stresses described in Supplementary Note 8. Both the total volumetric stresses of small particles before and after the martensitic transformation (σ_V^a, σ_V^b, respectively) show reasonable conformity with the Eshelby solution[37].

DISCUSSION

The lower M_s (Fig. 3b) and the lower transformation rate of the BMGCs with smaller nanocrystals (Fig. 3c), the initiation sites of martensitic transformation at the interface (Supplementary Fig. 6), and the remaining austenite adjacent to the crystalline-amorphous interface (Supplementary Fig. 7) all conform particularly well with the experimental results of Santamarta et al.[38,39] and Waitz et al.[40,41] (Supplementary Note 9). The nucleus of a newly precipitated R phase in nanosized B2 crystals can be considered as an R inclusion embedded in a small spherical B2 grain which resides inside an amorphous M phase matrix[42]. The change in free energy for the phase transformation ΔG_{MT} can be

written as:

$$\Delta G_{MT} = -V\Delta G_{B2 \to R} + E_{sto} - E_{pri}, \tag{5}$$

$$E_{sto} = E_{MT}^R + E_{MT}^{B2} + E_{MT}^M + E_{MT}^{R-B2} + E_{MT}^{B2-M} \tag{6}$$

$$E_{pri} = E_{el}^{B2} + E_{el}^M + E_{el}^{B2-M} \tag{7}$$

$$\Delta G_{MT} = -V\Delta G_{B2 \to R} + E_{sto} - (E_{el}^{B2} + E_{el}^M) - E_{el}^{B2-M} \tag{8}$$

$$\Delta G_{MT} = -V\Delta G_{B2 \to R} + E_{sto} + E_{el}^{B2}(\text{compressive}) + E_{el}^M(\text{compressive}) - E_{el}^{B2-M} \tag{9}$$

$$\Delta G_{MT} = -V\Delta G_{B2 \to R} + E_{sto} + E_{el}^{B2}(\text{compressive}) - E_{el}^M(\text{dilatative}) - E_{el}^{B2-M} \tag{10}$$

$$\Delta G_{MT} = -V\Delta G_{B2 \to R} + E_{sto} - E_{el}^{B2}(\text{dilatative}) - E_{el}^M(\text{dilatative}) - E_{el}^{B2-M} \tag{11}$$

where $\Delta G_{B2 \to R}$ is the change in free energy per unit volume when the B2 transforms into the R phase, and V is the volume of the newly precipitated R phase. E_{sto} is the stored energy arising from the strain energy and interfacial energy produced by the phase transformation; it generally includes the strain energy in the individual phases - R (E_{MT}^R), B2 (E_{MT}^{B2}), amorphous matrix M (E_{MT}^M), and the interface energies between R - B2 (E_{MT}^{R-B2}), and B2-M (E_{MT}^{B2-M}) per unit volume. E_{pri} refers to the elastic strain energy in B2 (E_{el}^{B2}), the amorphous matrix M (E_{el}^M), and the B2-M (the interfacial strain energy between B2 and the amorphous matrix M) (E_{el}^{B2-M}), prior to the phase transformation, respectively.

In Eq. (5), the first term $\Delta G_{B2 \to R}$, which is probably dependent on the temperature T and composition C, can be considered to remain constant per unit volume of the transformation from the B2 to the R phase. The second term, $E_{sto} = (E_{el}^{R} + E_{MT}^{B2} + E_{MT}^{M} + E_{MT}^{R-B2} + E_{MT}^{B2-M})$, should also be constant per unit volume for the transformation process from the B2 to the R phase. The third term, $E_{pri} = E_{el}^{B2} + E_{el}^{M} + E_{el}^{B2-M}$, consists of three terms: the elastic strain energy in the B2 (E_{el}^{B2}), the elastic strain energy in the amorphous matrix M (E_{el}^{M}), and the interfacial strain energy between the B2 and the amorphous matrix M (E_{el}^{B2-M}), prior to the phase transformation.

As the crystalline-amorphous interfacial energy E_{el}^{B2-M} acts as a promoter for phase transformation, it is always advantageous to decrease the Gibbs free energy of phase transformation. The absolute value of the interfacial energy increases with enlarged particle sizes (Supplementary Note 10 and Supplementary Fig. 8); therefore the nucleation barrier for bigger particles is much lower than that of the smaller particles. Equation (5) combined with Eq. (7) can be rewritten as Eq. (8), but the elastic strain energy in B2 (E_{el}^{B2}) and the amorphous matrix M (E_{el}^{M}) might inhibit or promote phase transformation depending on the innate strain gradient distribution.

For all specimens, the region directly adjacent to the interface of the B2 precipitates always possesses higher strain (Fig. 1f and Supplementary Fig. 3), stress (Fig. 1e) and potential energy (Fig. 2c and Supplementary Fig. 4). Therefore, the martensitic transformation (MT) will always initiate from the interface. When the "dL^{-1}" increases from 0.30 to 0.75 (Supplementary Fig. 3a–d), 0.85–0.94 (Supplementary Fig. 3e, f, to 0.94–1), the B2 phase and amorphous matrix sustains a large compressive strain (Fig. 4a1); the B2 phase is under 3D-compressive strain and the amorphous matrix experiences a dilatative strain (Fig. 4a2), whereas both the B2 and amorphous matrix adjacent to the interface experience a dilatative strain (Fig. 4a3). Compressive strains in all three dimensions will inhibit atomic shuffling and shape/volume change caused by the MT, while dilatative strains assist the transformation[43]. Accordingly, the compressive strain in the B2 precipitate will act as a prohibiting factor (Fig. 4a1, a2, Eqs. (9, 10)), with the dilatative strain assisting the transformation (Fig. 4a3, Eq. (11)). The compressive strain in the amorphous matrix (Fig. 4a1, Eq. (9)) will also increase the nucleation barrier of the MT, but the dilatative strain in the amorphous matrix can decrease this barrier for the MT (Figs. 4a2, 4a3, Eq. (10, 11)). A detailed description of this phenomenon is given in Supplementary Note 11.

From the above discussion, using Eqs. (9–11), we can summarize that the nucleation barrier for BMGCs with the smallest particles is the highest. The M_s temperature of BMGCs therefore exhibits a decreasing trend as the precipitate size decreases.

A schematic illustration of the innate elastic strain field is shown in Fig. 4. The correlation between the interfacial strain field and the nucleation and growth of the martensitic transformation for different B2 particle sizes is demonstrated in Fig. 4b, c. For BMGCs with smaller precipitates, both the compressive/dilatative transition region and the interfacial maximum strain are located outside the precipitate (Fig. 4a1). The center of the smaller precipitates undergoes higher compressive strain, and the amorphous matrix region surrounded by smaller precipitates encounters the smaller stress (Supplementary Fig. 3a–d and the upper panel in Fig. 4b, c). The nucleation barrier for the transformation is much higher than those with larger inclusions. For BMGCs with medium-sized precipitates, the compressive/dilatative transition region can be merged with the crystalline-amorphous interface (Fig. 4a2), while the interfacial maximum strain remains a few Ångstroms away from the interface (Supplementary Fig. 3e, f and middle panel in Fig. 4b, c). The compressive strain in the B2 particle decreases and the dilatative strain in the amorphous matrix increases as the B2 precipitate size becomes larger. The nucleation barrier for the MT is thus lower than that for BMGCs with smaller particles. For

BMGCs with very large precipitates, the location of the compressive/dilatative transition region is very close to, but might still be inside, the B2 precipitate (Fig. 4a3), while the maximum strain stays a few Ångstroms away from the interface and lower panel in Fig. 4b, c. The compressive strain in the B2 precipitate is the lowest whereas the dilatative strain in the amorphous matrix is the highest. The MT will be more likely to take place at higher temperatures or lower stresses. The redistribution of the strain field during MT is described in Supplementary Note 12 and Supplementary Fig. 10.

From the model proposed in Fig. 4, we can explain that it is ascribed to an enhanced transformed fraction of austenite precipitates such that shape-memory BMGCs can display even higher strength, better ductility, work-hardenability and impact toughness at cryogenic temperatures[18–21] (Supplementary Note 1). We can also explain the experimental results that larger B2 precipitates experience easier martensitic transformation (less strain is needed), while smaller B2 precipitates do not experience martensitic transformation due to the higher compressive strain surrounding the interface area when the B2 compounds form a bimodal size distribution inside the amorphous matrix[14]. Furthermore, with larger B2 precipitates it is also easier to promote shear band initiation due to the large inborn dilatative stress in the vicinity of the interface from the higher $\varepsilon_{max-interface}$. Smaller B2 precipitates cause an oscillation of the shear stress[14] as the location of maximum interfacial strain $\varepsilon_{max-interface}$ for smaller precipitates is further away from the interface compared to that for larger precipitates. If the morphological distribution of precipitates is Gaussian, considering the strain needed to overcome the innate compressive strain is lower for BMGCs embedded with larger precipitates, the first yield point of BMGCs containing particles with larger average diameters will probably occur at a lower stress, as is evident in the experimental work of Wu et al.[33].

In summary, an innate interfacial elastic strain gradient model of a transformable B2 precipitate embedded in an amorphous matrix based on MD simulations has been established. Compared to the Eshelby solution, this model proposes a nanometer scale interfacial region adjacent to the crystalline-amorphous interface which experiences gradient strain transitions from compressive to tensile. In this region, the crystalline-amorphous interface, the compressive/dilatative transition, and the interfacial maximum strain were characterized and differentiated instead of addressing them all as "interface" in a conventional fashion.

When the size of the spherical B2 precipitates gradually increases from small ($dL^{-1} < \sim 0.75$), medium-sized precipitates ($\sim 0.85 < dL^{-1} < \sim 0.94$) to very large precipitates ($\sim 0.94 < dL^{-1} < 1$), the compressive/dilatative transition region locates from inside the amorphous region to inside the B2 precipitate. The actual interface strain transits from compressive (for $dL^{-1} < \sim 0.91$) to dilatative (for $dL^{-1} > \sim 0.91$). The compressive (dilatative) stress state in the B2 precipitate and amorphous matrix serve to prohibit (assist) the initiation of martensitic transformation and increase (decrease) the nucleation barrier of the transformation. The looser (close-packed) interfacial interaction between the B2 precipitate and the amorphous matrix decreases (increases) the nucleation barrier of the transformation, thus increasing the M_s temperature.

The interfacial maximum strain, which is likely related to the "interfacial strain/stress concentration", is located a few Ångstroms away from the interface and inside the amorphous matrix, instead of at the "exact" interface. The value of the "interfacial stress concentration" is always higher than the strain at the "exact" interface and increases as the precipitate sizes in the BMGCs are enlarged. By properly manipulating the transformation fraction of the martensitic transformation and interfacial stress concentration, the "transformation-mediated work hardening and plasticity" effect can be maximized to overcome the strength-ductility trade-off even at cryogenic temperatures.
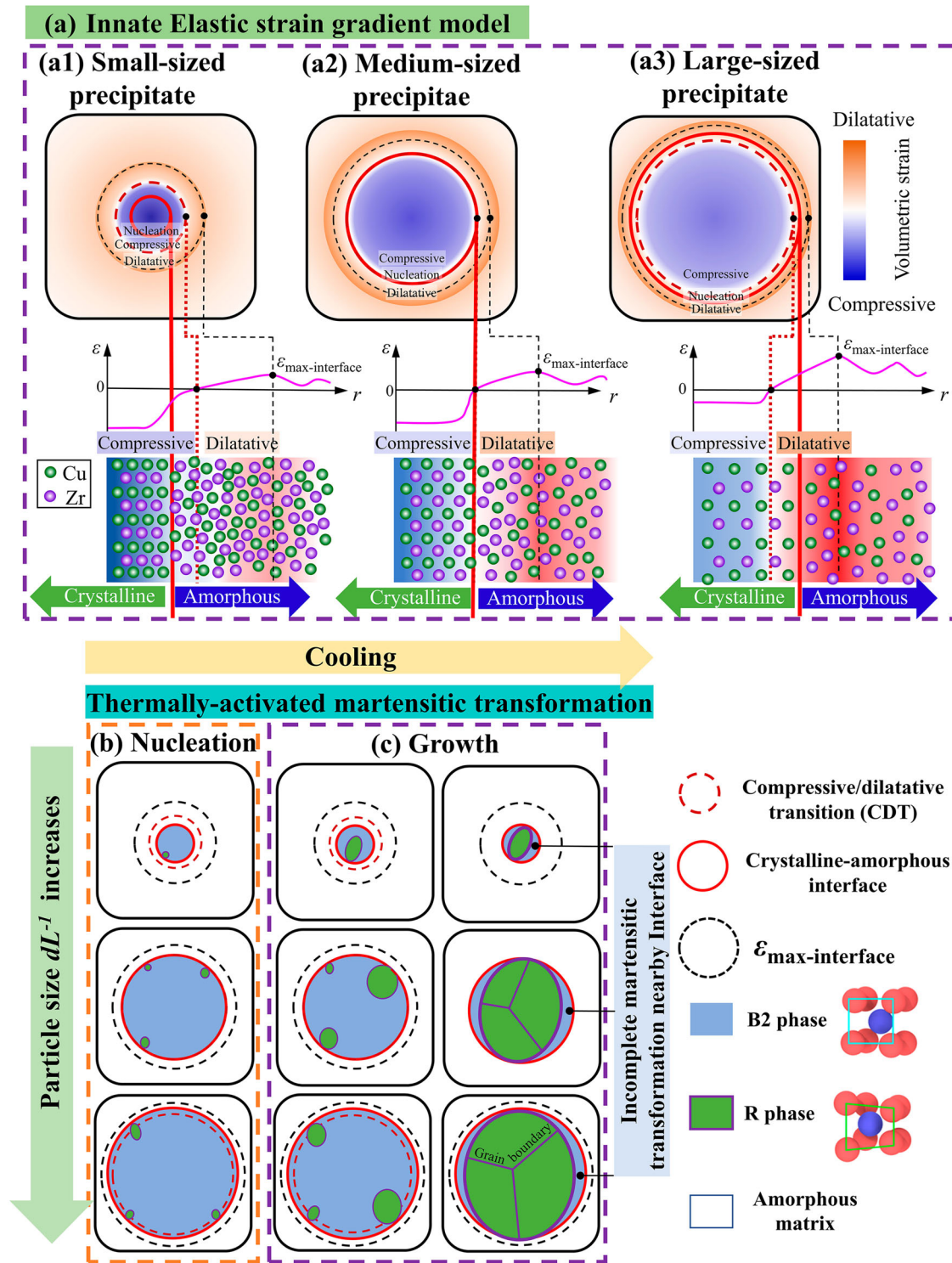
Fig. 4 The innate interfacial strain gradient model for various sized precipitate enhanced metallic-glass composites. a Schematic illustration of the elastic strain gradient effect of a1) small-sized a2) medium-sized a3) large-sized spherical-shaped B2 nanoparticles embedded in an amorphous matrix, indicating the relative position of the compressive/dilatative transition, the crystalline-amorphous interface and the interfacial maximum strain $\varepsilon_{max-interface}$. The position of the compressive/dilatative transition moves from (a1) inside amorphous region to (a2) merge with the interface to (a3) inside B2 precipitate; the interfacial maximum strain is always located inside the amorphous matrix. As the particle size increases, the distance between the interfacial maximum strain and the interface becomes smaller. **b** Illustrations of the initial nucleation sites at the nearby-interface layer inside the B2 precipitate, and (**c**) the growth processes of the R phase undergoing martensitic transformation.

METHODS

MD simulations

This problem was investigated with MD simulations using the open source LAMMPS package[44], employing the recently developed Cu-Zr embedded atom method (EAM) potential by Mendelev et al.[45]. The potential is the latest development with some reasonably semi-empirical corrections from previous potentials[46], which show reproducible results with X-ray diffraction measurement data on amorphous alloys. Indeed, the EAM potential has been successful in elucidating many phase transformation related phenomena[47–49]. 3D periodic boundary conditions were applied to avoid surface effects[50]. For all simulations, a constant integration time step of 1 fs was used. The isobaric-isothermal (NPT) ensemble at zero external pressure was applied to the system. The Nosé-Hoover thermostat[51,52] and the Parrinello-Rahman barostat[53] were utilized to control the temperature and pressure. Atomic visualization and analysis were performed using OVITO software[54], in which the crystal structures were identified by a polyhedral template matching algorithm (PTM)[55].

A $Cu_{50}Zr_{50}$ single crystal block (~686,000 atoms) was prepared with a cell size of 23 nm along the crystallographic directions of [100], [010] and [001]. To construct the composite (Fig. 1a–c), the sample was divided into two sectors: the spherical area was addressed as the "crystalline region" (yellowed colored area in Fig. 1a–c), with the rest of the composite as the "amorphous region" (blue-red colored area in Fig. 1a–c). The "amorphous region" atoms were selected and melted at 2000 K. After thermalizing at 2000 K for 0.2 ns, these atoms were quenched to 300 K at a cooling rate of $1\,Kps^{-1}$ in the NPT (isobaric-isothermal) ensemble to achieve the glassy state. The "amorphous region" was then relaxed at 300 K for 0.2 ns. This created the unrelaxed atomic configuration of the composite (Fig. 1c, left side). The entire composite was then relaxed at 300 K for 0.2 ns to acquire the relaxed atomic configuration (Fig. 1c, right side). After relaxation, no obvious voids (e.g., defects, dislocations) were observed near the crystalline-amorphous interface. The number of atoms in the crystal and amorphous regions, the associated volume percentages of the B2 phase and the surface to volume ratio of the B2 crystals relative to the BMGCs are listed in Supplementary Table 1.

To simulate the thermally-activated martensitic transformation, all samples were heated from 300 K to 500 K at a heating rate of $1\,Kps^{-1}$, and annealed at 500 K for 0.3 ns, prior to cooling from 500 K to 70 K at a rate of $-0.5\,Kps^{-1}$ to induce the B2-R martensite transformation. It should be noted that the temperature rise from 300 K to 500 K is unlikely to have a notable impact on the innate strain distribution; these small raises were to assure that the martensitic transformation was observable in this work.

DATA AVAILABILITY

The data that support the findings of this study are available from the corresponding authors upon request.

CODE AVAILABILITY

The computational code used in this study is available upon request from Xiaoling Fu.

REFERENCES

1. Sun, B. A. & Wang, W. H. The fracture of bulk metallic glasses. *Prog. Mater. Sci.* **74**, 211–307 (2015).
2. Cheng, Y. Q. & Ma, E. Atomic-level structure and structure–property relationship in metallic glasses. *Prog. Mater. Sci.* **56**, 379–473 (2011).
3. Hufnagel, T. C., Schuh, C. A. & Falk, M. L. Deformation of metallic glasses: Recent developments in theory, simulations, and experiments. *Acta Mater.* **109**, 375–393 (2016).
4. Qiao, J., Jia, H. & Liaw, P. K. Metallic glass matrix composites. *Mater. Sci. Eng. R: Rep.* **100**, 1–69 (2016).
5. Fu, X. et al. Compressive ductility and fracture resistance in CuZr-based shape-memory metallic-glass composites. *Int. J. Plast.* **128**, 102687 (2020).
6. Oh, Y. S., Kim, C. P., Lee, S. & Kim, N. J. Microstructure and tensile properties of high-strength high-ductility Ti-based amorphous matrix composites containing ductile dendrites. *Acta Mater.* **59**, 7277–7286 (2011).
7. Hofmann, D. C. et al. Designing metallic glass matrix composites with high toughness and tensile ductility. *Nature* **451**, 1085–1089 (2008).
8. Hofmann, D. C. et al. Development of tough, low-density titanium-based bulk metallic glass matrix composites with tensile ductility. *Proc. Natl. Acad. Sci.* **105**, 20136–20140 (2008).
9. Pauly, S., Gorantla, S., Wang, G., Kuhn, U. & Eckert, J. Transformation-mediated ductility in CuZr-based bulk metallic glasses. *Nat. Mater.* **9**, 473–477 (2010).
10. Chen, Y., Tang, C. & Jiang, J.-Z. Bulk metallic glass composites containing B2 phase. *Prog. Mater. Sci.* **121**, 100799 (2021).
11. Song, W. L. et al. Microstructural control via copious nucleation manipulated by in situ formed nucleants: large-sized and ductile metallic glass composites. *Adv. Mater.* **28**, 8156–8161 (2016).
12. Zhang, L. et al. Strain-induced structural evolution of interphase interfaces in CuZr-based metallic-glass composite reinforced by B2 crystalline phase. *Compos. B: Eng.* **258**, 110698 (2023).
13. Wu, Y., Xiao, Y. H., Chen, G. L., Liu, C. T. & Lu, Z. P. Bulk metallic glass composites with transformation-mediated work-hardening and ductility. *Adv. Mater.* **22**, 2770–2773 (2010).
14. Hong, S. H. et al. Combinatorial influence of bimodal size of B2 TiCu compounds on plasticity of Ti-Cu-Ni-Zr-Sn-Si bulk metallic glass composites. *Metall. Mater. Trans. A* **45**, 2376–2381 (2014).
15. Zhang, L. et al. Cooperative shear in bulk metallic glass composites containing metastable b-Ti dendrites. *Phys. Rev. Lett.* **125**, 055501 (2020).
16. Zhang, L. et al. Tuning the microstructure and metastability of β-Ti for simultaneous enhancement of strength and ductility of Ti-based bulk metallic glass composites. *Acta Mater.* **168**, 24–36 (2019).
17. Zhang, J. et al. Strengthening Ti-based bulk metallic glass composites containing phase transformable β-Ti via Al addition. *Scr. Mater.* **173**, 11–15 (2019).
18. Jiang, S. et al. Temperature-dependent deformation behavior of a CuZr-based bulk metallic glass composite. *J. Alloys Compd.* **858**, 158368 (2021).
19. Zhang, L. et al. On low-temperature strength and tensile ductility of bulk metallic glass composites containing stable or shape memory β-Ti crystals. *Acta Mater.* **222**, 117444 (2022).
20. Li, G. et al. Stability of a metastable B2 phase embedded in a metallic glass matrix at liquid-nitrogen temperature. *Mater. Sci. Eng. A* **634**, 99–102 (2015).
21. Yan, T. et al. Temperature-dependence of impact toughness of bulk metallic glass composites containing phase transformable β-Ti crystals. *Acta Mater.* **229**, 117827 (2022).
22. Eshelby, J. D. The determination of the elastic field of an ellipsoidal inclusion, and related problems. *Proc. R. Soc. Lond. A, Math. Phys. Sci.* **241**, 376–396 (1957).
23. Hong, S. H. et al. Gradual martensitic transformation of B2 phase on TiCu-based bulk metallic glass composite during deformation. *Intermetallics* **75**, 1–7 (2016).
24. Zhang, Z. Y. et al. Effects of Sn addition on phase formation and mechanical properties of TiCu-based bulk metallic glass composites. *Intermetallics* **42**, 68–76 (2013).
25. Jiang, S. et al. In situ study of the shear band features of a CuZr-based bulk metallic glass composite. *Intermetallics* **112**, 106523 (2019).
26. Sun, H. C. et al. In-situ tensile testing of ZrCu-based metallic glass composites. *Sci. Rep.* **8**, 4651 (2018).
27. Schryvers, D., Tirry, W. & Yang, Z. Q. Measuring strain fields and concentration gradients around Ni_4Ti_3 precipitates. *Mater. Sci. Eng. A* **438–440**, 485–488 (2006).
28. Tirry, W. & Schryvers, D. Quantitative determination of strain fields around Ni_4Ti_3 precipitates in NiTi. *Acta Mater.* **53**, 1041–1049 (2005).
29. Tirry, W. & Schryvers, D. Linking a completely three-dimensional nanostrain to a structural transformation eigenstrain. *Nat. Mater.* **8**, 752–757 (2009).
30. Chowdhury, P., Patriarca, L., Ren, G. & Sehitoglu, H. Molecular dynamics modeling of NiTi superelasticity in presence of nanoprecipitates. *Int. J. Plast.* **81**, 152–167 (2016).
31. Li, Z. et al. Atomic scale modeling of the coherent strain field surrounding Ni_4Ti_3 precipitate and its effects on thermally-induced martensitic transformation in a NiTi alloy. *Acta Mater.* **211**, 116883 (2021).
32. Lyu, G.-J. et al. Microstructural effects on the dynamical relaxation of glasses and glass composites: a molecular dynamics study. *Acta Mater.* **220**, 117293 (2021).
33. Wu, Y. et al. Transformation-induced plasticity in bulk metallic glass composites evidenced by in-situ neutron diffraction. *Acta Mater.* **124**, 478–488 (2017).

34. Shi, Y. & Falk, M. L. A computational analysis of the deformation mechanisms of a nanocrystal–metallic glass composite. *Acta Mater.* **56**, 995–1000 (2008).

35. Ko, W.-S., Grabowski, B. & Neugebauer, J. Impact of asymmetric martensite and austenite nucleation and growth behavior on the phase stability and hysteresis of freestanding shape-memory nanoparticles. *Phys. Rev. Mater.* **2**, 030601 (2018).

36. Song, K. et al. In situ high-energy X-ray diffraction study of thermally-activated martensitic transformation far below room temperature in CuZr-based bulk metallic glass composites. *J. Alloys Compd.* **841**, 155781 (2020).

37. Sun, B. A. et al. Transformation-mediated plasticity in CuZr based metallic glass composites: a quantitative mechanistic understanding. *Int. J. Plast.* **85**, 34–51 (2016).

38. Santamarta, R. & Schryvers, D. Microstructure of a partially crystallised $Ti_{50}Ni_{50}Cu_{25}$ Melt-Spun Ribbon. *Mater. Trans.* **44**, 1760–1767 (2003).

39. Santamarta, R. & Schryvers, D. Effect of amorphous–crystalline interfaces on the martensitic transformation in $Ti_{50}Ni_{25}Cu_{25}$. *Scr. Mater.* **50**, 1423–1427 (2004).

40. Waitz, T., Antretter, T., Fischer, F. D., Simha, N. K. & Karnthaler, H. P. Size effects on the martensitic phase transformation of NiTi nanograins. *J. Mech. Phys. Solids* **55**, 419–444 (2007).

41. Waitz, T. & Karnthaler, H. P. Martensitic transformation of NiTi nanocrystals embedded in an amorphous matrix. *Acta Mater.* **52**, 5461–5469 (2004).

42. Meng, Q., Rong, Y. & Hsu, T. Y. Nucleation barrier for phase transformations in nanosized crystals. *Phys. Rev. B* **65**, 174118 (2002).

43. Jacobus, K., Sehitoglu, H. & Balzer, M. Effect of stress state on the stress-induced martensitic transformation in polycrystalline Ni-Ti alloy. *Metall. Mater. Trans. A* **27**, 3066–3073 (1996).

44. Plimpton, S. Fast parallel algorithms for short-range molecular dynamics. *J. Comput. Phys.* **117**, 1–19 (1995).

45. Mendelev, M., Sun, Y., Zhang, F., Wang, C.-Z. & Ho, K.-M. Development of a semi-empirical potential suitable for molecular dynamics simulation of vitrification in Cu-Zr alloys. *J. Chem. Phys.* **151**, 214502 (2019).

46. Mendelev, M. I., Sordelet, D. J. & Kramer, M. J. Using atomistic computer simulations to analyze x-ray diffraction data from metallic glasses. *J. Appl. Phys.* **102**, 043501 (2007).

47. Yuan, S., Song, X. & Branicio, P. S. Tuning the mechanical properties of shape memory metallic glass composites with brick and mortar designs. *Scr. Mater.* **186**, 69–73 (2020).

48. Sutrakar, V. K. & Mahapatra, D. R. Stress-induced martensitic phase transformation in Cu–Zr nanowires. *Mater. Lett.* **63**, 1289–1292 (2009).

49. Şopu, D., Albe, K. & Eckert, J. Metallic glass nanolaminates with shape memory alloys. *Acta Mater.* **159**, 344–351 (2018).

50. Şopu, D. & Albe, K. Influence of grain size and composition, topology and excess free volume on the deformation behavior of Cu–Zr nanoglasses. *Beilstein J. Nanotechnol.* **6**, 537–545 (2015).

51. Nosé, S. A unified formulation of the constant temperature molecular dynamics methods. *J. Chem. Phys.* **81**, 511–519 (1984).

52. Hoover, W. G. Canonical dynamics: equilibrium phase-space distributions. *Phys. Rev. A* **31**, 1695 (1985).

53. Parrinello, M. & Rahman, A. Polymorphic transitions in single crystals: a new molecular dynamics method. *J. Appl. Phys.* **52**, 7182–7190 (1981).

54. Stukowski, A. Visualization and analysis of atomistic simulation data with OVITO–the Open Visualization Tool. *Model. Simul. Mat. Sci. Eng.* **18**, 015012 (2009).

55. Larsen, P. M., Schmidt, S. & Schiøtz, J. Robust structural identification via polyhedral template matching. *Model. Simul. Mat. Sci. Eng.* **24**, 055007 (2016).

AUTHOR CONTRIBUTIONS

COMPETING INTERESTS

The authors declare no competing interests.

ADDITIONAL INFORMATION

Supplementary information The online version contains supplementary material available at https://doi.org/10.1038/s41524-023-01182-6.

Correspondence and requests for materials should be addressed to Xiaoling Fu or Robert O. Ritchie.

Reprints and permission information is available at http://www.nature.com/reprints

Publisher's note Springer Nature remains neutral with regard to jurisdictional claims in published maps and institutional affiliations.